

Article

The Photocatalytic Degradation of Vehicle Exhausts by an Fe/N/Co–TiO₂ Waterborne Coating under Visible Light

Huiyun Xia ^{*}, Guanyu Liu, Rui Zhang, Lifang Song  and Huaxin Chen ^{*}

Engineering Research Center of Transportation Materials of Ministry of Education, School of Materials Science and Engineering, Chang'an University, Xi'an 710064, China; lgy16602912220@163.com (G.L.); dykcsjzr@163.com (R.Z.); slf@chd.edu.cn (L.S.)

^{*} Correspondence: xiahy@chd.edu.cn (H.X.); hxchen@chd.edu.cn (H.C.); Tel.: +86-029-8233-7246 (H.C.)

Received: 15 September 2019; Accepted: 14 October 2019; Published: 16 October 2019



Abstract: Based on the three-dimensional network structure of a polymer and the principle of photocatalysts, a visible-light-responsive and durable photocatalytic coating for the degradation of vehicle exhaust (VE) has been constructed using a waterborne acrylic acid emulsion as the coating substrate; Fe/N/Co–TiO₂ nanoparticles (NPs) as photocatalytic components; and water, pigments, and fillers as additives. The visible-light-responsive Fe/N/Co–TiO₂ NPs with an average size of 100 nm were prepared by sol-gel method firstly. The co-doping of three elements extended the absorption range of the modified TiO₂ nanoparticles to the visible light region, and showed the highest light absorption intensity, which was confirmed by the ultraviolet-visible absorption spectra (UV-Vis). X-ray diffraction (XRD) measurements showed that element doping prevents the transition from anatase to rutile and increases the transition temperature. TiO₂ was successfully doped due to the reduction of the chemical binding energy of Ti, as revealed by X-ray photoelectron spectroscopy (XPS). The degradation rates of NO_x, CO, and CO₂ in VE by Fe/N/Co–TiO₂ NPs under visible light were 71.43%, 23.79%, and 21.09%, respectively. In contrast, under the same conditions, the degradation efficiencies of coating for VE decreased slightly. Moreover, the elementary properties of the coating, including pencil hardness, adhesive strength, water resistance, salt, and alkali resistance met the code requirement. The photocatalytic coating exhibited favorable reusability and durability, as shown by the reusability and exposure test.

Keywords: photocatalytic degradation; doped nano-TiO₂; vehicle exhaust; waterborne acrylic coating; visible light

1. Introduction

With the rapid development of highway transportation and urban construction in the world, vehicle exhaust (VE) has gradually become the main source of air pollution in the world [1–3]. During recent decades, with the control of policies, the emission of air pollution in the world was considerably reduced [4,5]; however, the concentration of air pollutants is still high, especially in traffic-intensive urban areas [6–9]. At the same time, hazardous substances, such as CO, CO₂, NO_x, HC and other components in the VE cause haze and photochemical smog, both of which seriously damage human health [10–14].

At present, the methods commonly used to degrade VE mainly include physical adsorption [15], catalytic degradation [16–19], and soil VE purification [20,21]. Because of the chemical and thermal stability, high refractive index, nontoxicity, and wide band gap energy of TiO₂ [22–24], it has been used as one kind of light harvester in the areas of air purification, water treatment, and deodorization [13].

Moreover, TiO₂ was adopted as a photocatalytic material to purify VE in the areas of ceramics, concrete, and pavement [16,17]. In 1999, TiO₂ was first used in cement pavement to degrade NO_x discharged from automobiles in Japan, and the results showed that TiO₂ could purify NO_x in VE [19]. Leng and Yu [9] coated TiO₂ particles on an asphalt pavement surface to purify NO_x in VE, and the durability of coating was evaluated. It is worth mentioning that in most of the above studies, TiO₂ particles were incorporated into the asphalt and cement concretes to achieve efficient degradation of VE. However, this method is only applicable to new sections of road and buildings, not to existing sections. Therefore, its scope of application is limited.

As a kind of functional material, photocatalytic coatings have the advantages of simple construction, low cost, wide application, and high photocatalytic degradation of pollutants. Xu et al. [25] prepared a photocatalytic coating using an anti-corrosion coating with TiO₂ and found that it had the effect of degrading Pirola et al. [26] prepared composite photocatalytic materials based four different matrix materials and coated them on the exterior walls of buildings. The degradation ability of silicate photocatalysts after one year is lower than that of siloxane photocatalysts. Martinez et al. [27] reported NO degradation properties with a polymer coating carrying TiO₂ nanoparticles. However, few studies have reported the application of photocatalytic coatings in some special environments, such as tunnels with high VE concentration and weak internal light intensity [28].

Gallus et al. [29] reported three different methods to quantify the ability of photocatalytic coatings to degrade tunnel pollutants. Coating degradation efficiency was measured before or after application, upwind or downwind of the test section, and with UV lamps on or off. Guerrini [30] found that the concentration of NO_x in the same position decreased by more than 50% compared with that before and after coating. This study demonstrates the feasibility of photocatalytic coatings used to degrade exhaust gas in tunnels. However, an ultraviolet light source was used as the excitation source in the above studies of tunnels; in fact, only visible light is available in tunnels at present. Therefore, the degradation effect and performance of the photocatalytic coatings need to be further studied.

The main objective of this research was to develop a photocatalytic waterborne coating which can degrade VE effectively under visible light, so the performance of photocatalytic coating was characterized. In this study, the visible light responsive Fe/N/Co–TiO₂ photocatalyst was prepared by the sol-gel method. The effect of doping elements on crystal structure and photocatalytic ability was studied. A visible-light-responsive and durable photocatalytic coating was constructed by using acrylic acid waterborne emulsion as the coating substrate; Fe/N/Co–TiO₂ nanoparticles as photocatalytic components; and water, pigments, and fillers as additives. The photocatalytic performance of the coating under ultraviolet and visible light was characterized by self-made degradation test chamber. The reusability of VE degradation was studied by cyclic degradation test and durability test.

2. Experimental

2.1. Materials and Reagents

Titanium (IV) butoxide (TBOT, 99%) was purchased from Tianjin Kemiou Chemical Reagent Co., Ltd. (Tianjin, China). Absolute ethanol (99%) and ammonia solution (NH₄OH, 28%) was purchased from Tianjin Fuyu Fine Chemical Co., Ltd. (Tianjin, China). Nitric acid (HNO₃, 65%) was purchased from Chengdu Kelon Chemical Reagent Factory (Chengdu, China). Ferric nitrate (Fe(NO₃)₃·9H₂O, 98%) and cobalt nitrate (Co(NO₃)₂·6H₂O, 99%) were purchased from Sinopharm Chemical Reagent Co., Ltd. (Shanghai, China). Urea (99%) was purchased from Tianjin Fuchen Chemical Reagent Factory (Tianjin, China). Sodium hydroxymethyl cellulose (99%), hexametaphosphate (99%), talcum powder (99%), and barium sulfate (99%) were purchased from Tianjin Guangfu Fine Chemical Research Institute (Tianjin, China). Rutile titanium dioxide (94%) was purchased from Shanghai Coking Group Titanium Dioxide Factory (Shanghai, China). Acrylic emulsion was purchased from Guangzhou Rongdong Chemical Co., Ltd. (Guangzhou, China).

2.2. Preparation of Fe/N/Co–TiO₂

Fe/N/Co–TiO₂ catalyst samples were synthesized using the sol-gel method. Specific steps are as follows:

Firstly, 140 mL anhydrous ethanol was blended with 10 mL glacial acetic acid in a 500 mL glass beaker at room temperature. Then, 30 mL of TBOT was slowly added while stirring was continued for 20 min.

Secondly, the pH of the above mixture was adjusted to 2 by adding 3 mL nitric acid; after that, 60 mL of deionized water was added. The modified TiO₂ sol was prepared by adding 1.527 g of Fe(NO₃)₃, 2.574 g of CO(NH₂)₂, and 2.502 g of Co(NO₃)₂, and stirring at a high speed for 30 min. The sol was aged for 3 days at room temperature to prepare gel.

Thirdly, the prepared sol was added to the flask and placed in a rotary evaporator to evaporate the solvent completely. The solid gel was dried in a blast drying oven at 100 °C to obtain a dry gel, and then it was ground into powder.

Finally, the prepared powder was calcined at different calcination temperatures (550 °C, 600 °C, and 650 °C) for 2 h in the muffle furnace to obtain Fe/N/Co–TiO₂.

According to the above method, Fe–TiO₂ was synthesized by adding an appropriate amount of Fe(NO₃)₃. Fe/N–TiO₂ was synthesized by adding appropriate amount of Fe(NO₃)₃ and CO(NH₂)₂ in the preparation of modified sol. TiO₂ was synthesized by the same preparation method without doping.

2.3. Preparation of the Photocatalytic Coating

Firstly, 0.5 g of sodium carboxymethylcellulose was dispersed in 25 mL water to form an aqueous solution. After adding 10 g of Fe/N/Co–TiO₂, 10 g of rutile TiO₂, 2.5 g of BaSO₄, 2.5 g of talcum powder, and 0.5 g of hexametaphosphate, the paint disperser, were used for dispersion for 1 h at 30 rpm. The mixture was called liquid A. Secondly, 40 g waterborne acrylic emulsion was blended with 5 g of 2,2,4-trimethyl 1,3-pentanediol monoisobutyrate, and the pH of mixture was adjusted to 7–8 by adding aqueous ammonia solution; the above mixture was named liquid B. Thirdly, the coating was prepared by mixing liquids A and B with a small amount of defoamer and a leveling agent at 18 rpm for 0.5 h continuously. Finally, the coating was screened by a 200 mesh screen, then coated on the surface of q non-cotton fiber cement board (150 mm × 70 mm), and dried at room temperature.

2.4. Characterization

Colloidal particle sizes of samples were detected by Zetasizer nanoparticle size analyzer (Malvern Zetasizer Nano, Malvern, UK). The crystalline phases of samples were identified by X-ray diffraction analysis (Bruker AS, Inc., D8ADVANCE, Karlsruhe, Germany) with Cu-K α operating at 40 kV and 40 mA. The scan rate was 0.2°/s and in the range of 15°–80°. The morphology of sample was observed using transmission electron microscopy (TEM, JEM-2100F, JEOL, Tokyo, Japan) with a test voltage of 200 kV. The TEM samples were prepared by sonication of the photocatalyst powders in ethanol for 15 min, and subsequently, dropping the dispersion onto carbon copper grids. The chemical bonding state of samples was measured by XPS (AXIS ULTRA, KRATOS, Manchester, UK) with a monochromatic Al-K α X-ray source (KE = 1486.6 eV, 150 W). All XPS spectra were corrected by the C1s peak of external hydrocarbon contamination located at 284.8 eV. The UV-Vis diffuse reflectance spectra were measured by UV-Vis spectrophotometer equipped with an integrated sphere (UV 3600, Shimadzu Corporation, Kyoto, Japan). The reference material of the sample was BaSO₄ and the test wavelength range was 200–800 nm.

2.5. Photocatalytic Degradation Experiment

The photocatalytic performances of Fe, Fe/N, and Fe/N/Co–TiO₂ were measured by the degradation of methylene blue (MB) and VE. The photocatalytic performance of the coating was measured by VE degradation experiment.

2.5.1. The Photocatalytic Degradation Experiment with MB

Firstly, 100 mg of the prepared catalyst was added to 100 mL of a 10 mg/L MB solution in a 250 mL double-layered beaker, which could be passed into cooling water to maintain the reaction temperature. The mixture was stirred in the dark for 30 min to adsorb MB. Next, photocatalytic degradation was initiated by turning on a 300 W xenon lamp that filtered out ultraviolet rays. In total, 3 mL of the reaction solution was placed in a centrifuge tube, and centrifuged for 8 min at 3000 rpm. The upper supernatant was separated and the data of MB absorbance were recorded by UV spectrometer at a wavelength (λ) of 650 nm. The degree of MB absorbance decrease was regarded as the evaluation index of photocatalytic degradation ability, which was calculated by Equation (1).

$$\eta = \frac{C_0 - C}{C_0} \times 100\% = \frac{A_0 - A}{A_0} \times 100\% \quad (1)$$

where η is the degradation efficiency of MB, C_0 is the initial concentration of MB, and C is the residual concentration after photocatalytic reaction.

2.5.2. The Photocatalytic Degradation Experiment of VE

The photocatalytic degradation experiment of VE was carried out by a self-made photocatalytic VE reaction chamber (Figure 1) at room temperature. The VE was from a professional preparation of Jining Xieli Special Gas Co., Ltd. (Xi'an, China) The reaction chamber was made of plexiglass, equipped with fans for dispersing gases, ultraviolet and visible light sources, and a platform for loading samples. The air tightness of the reaction chamber was ensured during the experiment, otherwise the experimental results would have been affected. The NHA-506 VE analyzer manufactured by Nantong Huapeng Electronics Co., Ltd. (Nantong, China) was used in the experiment. To ensure the accuracy of the experimental results, test errors of VE reaction chamber and VE analyzer were calibrated.



Figure 1. The photocatalytic vehicle exhaust (VE) reaction chamber.

Firstly, 2.0 g of Fe/N/Co-TiO₂ was evenly distributed in ethanol, and the above dispersions were placed in four, 95 mm Petri dishes and dried in an oven. Next, the prepared Fe/N/Co-TiO₂ or coating sample plate (8 pieces) was placed in the reaction chamber. The reaction chamber was sealed with a sealed cover and shielded it to avoid the Fe/N/Co-TiO₂ or coating being irradiated by external light source. Leakage detection was performed before VE was introduced into the closed reactor. Subsequently, VE was introduced until the desired concentration was reached and the fan was turned

on to disperse the gas evenly. Finally, UV or a visible light source in the reaction chamber was turned on, and the concentration of each component (including CO, CO₂, and NO_x) was recorded every 20 min by NHA-506 VE analyzer. The photocatalytic degradation abilities of the samples were evaluated by the degradation rates of VE's concentration in the reaction chamber. The formula used was the same as that of Equation (1).

3. Results and Discussion

3.1. The Crystal Structures and Optical Properties of the Photocatalysts

3.1.1. The Effect of Doping Elements on Colloidal Particle Size

To investigate the effect of element species on the particle size distribution of colloidal Fe/N/Co-TiO₂, modified TiO₂ nanoparticles (NPs) doped with different elements were prepared, and their particle size distributions are shown in Figure 2. Compared with the TiO₂ colloid, the particle size distributions of Fe-TiO₂, Fe/N-TiO₂, and Fe/N/Co-TiO₂ colloids became narrow; the average particle sizes of sols were 11.15, 9.56, and 10.64 nm, respectively, as shown in Table 1.

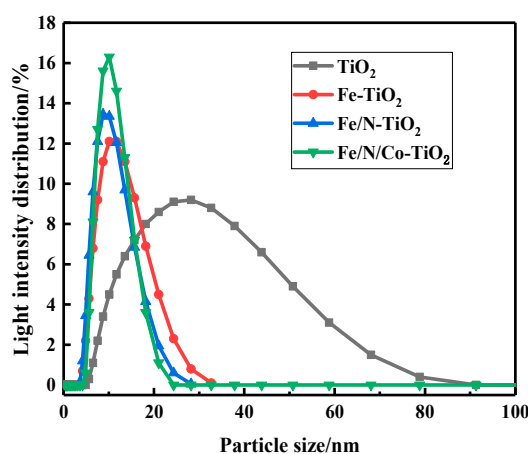


Figure 2. The particle size distribution of doped-TiO₂ with different doping elements.

Table 1. The colloidal particle size of Fe, Fe/N, and Fe/N/Co-TiO₂.

Number	Doping Element	Average Particle Size/nm	Distribution Coefficient (PDI)
1	Undoped	36.10	0.349
2	Fe	11.15	0.240
3	Fe/N	9.56	0.179
4	Fe/N/Co	10.64	0.204

These phenomena may be related to Brownian motion [31]. When a certain amount of Fe³⁺ is incorporated into the TiO₂ colloid, the replacement of Ti⁴⁺ by Fe³⁺ makes the Fe-TiO₂ colloid negatively charged. The Fe-TiO₂ colloids with the same charge have a repulsion effect, so the colloids are unlikely to coagulate and the particle size becomes smaller [32]. N was adopted as a non-metallic element to provide more negative charge, thus making the particle size smaller [33]. Since the doping of Co²⁺ breaks the charge balance again, the colloidal motion is intensified, and the colloidal particle size is increased.

3.1.2. The Effect of Doping Elements on UV-Vis

To investigate the effect of elemental species on the optical absorption ability of Fe/N/Co-TiO₂ NPs, the optical absorption properties of doped TiO₂ were characterized by UV-Vis spectra. In reference to

Figure 3a, it can be seen that: (i) The doping made the absorption range extend to the visible light region. (ii) The absorption intensity of doped TiO_2 in the ultraviolet light and visible light regions increased obviously compared with un-doped TiO_2 . (iii) The Fe/N/Co-TiO_2 showed the most obvious red shift of absorption edge and highest absorption intensity among the doped TiO_2 NPs in the visible region. Furthermore, the band gap values of TiO_2 , Fe-TiO_2 , Fe/N-TiO_2 , and Fe/N/Co-TiO_2 NPs were 3.2, 2.6, 2.3, and 2.1 eV estimated by Kubelka–Munk function (c.f. Figure 3b). This indicates that the band gap width decreases significantly after doping, which is more conducive to improving the visible light response's efficiency. It can be concluded that tri-doping plays an important synergistic role in the absorption of TiO_2 in the visible region [34].

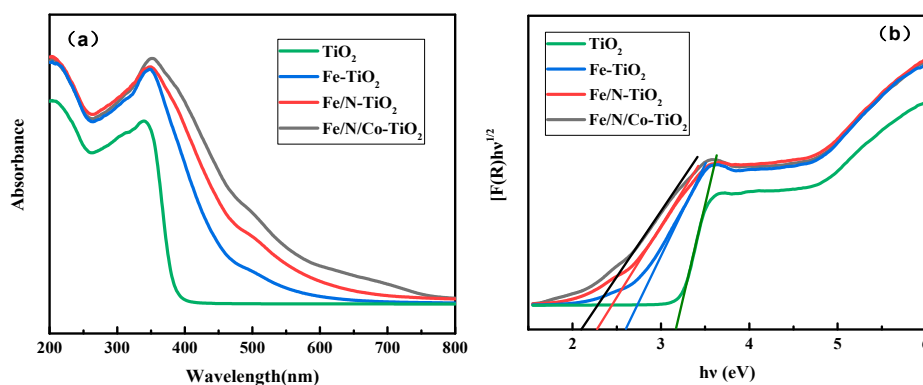


Figure 3. The UV-Vis absorption (a) and corresponding plot of transformed Kubelka–Munk function pattern (b) of TiO_2 , Fe , Fe/N , and Fe/N/Co-TiO_2 particles after calcination at 650°C .

The expansion of Fe-TiO_2 adsorption under visible light comes from the electronic transition from the dopant energy level ($\text{Fe}^{3+}/\text{Fe}^{4+}$) to the conduction band of TiO_2 [35–37]. However, the mechanisms of photoexcitation changes induced by doping with Fe or N are different. The TiO_2 band gap narrowing is induced by the localized N 2p states (acceptor states) positioned above the TiO_2 valence band when N is incorporated in TiO_2 lattice [38]. The charge separation is promoted, so the band gap is further reduced. Therefore, Fe/N-TiO_2 can be activated with much longer wavelengths than Fe-TiO_2 [39]. It is reported that the substitution of Co^{2+} to Ti^{4+} in TiO_2 crystals causes lattice defects and breaks the electron and hole motion states [40], which may arise from charge transfer and d–d transitions [41], leading to a further red shift. Thereby, the photoactivity of Fe/N/Co-TiO_2 is further improved by tri-doping and exhibits more excellence in the visible region.

3.1.3. The Effect of Calcination Temperature on XRD of Fe/N/Co-TiO_2

To investigate the effect of calcination temperature on the crystal structure, the XRD pattern of Fe/N/Co-TiO_2 at different calcination temperatures were measured. Figure 4 shows the XRD patterns of Fe/N/Co-TiO_2 at different calcination temperatures. The typical anatase TiO_2 patterns appear at 2θ of 25.3° , 37.8° , 48.0° , 53.9° , and 62.68° , and rutile TiO_2 appears at 2θ of 27.4° and 36.1° . After calcination at 550°C , the crystal form of undoped TiO_2 is a mixture of anatase and rutile. However, Fe/N/Co-TiO_2 is anatase, there is no rutile. This is because the doping of Fe and N inhibits the growth of crystallite, and the transition from anatase to rutile is prevented, transition temperature increased [42,43].

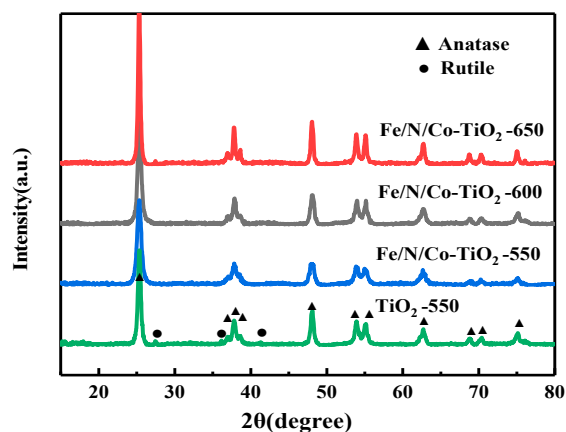


Figure 4. The XRD patterns of doped-TiO₂ after calcination at different temperatures.

The diffraction peak of anatase of Fe/N/Co-TiO₂ became sharper as the calcination temperature increased, and the rutile peaks appeared when the calcination temperature reached 650 °C. It is also indicated that with the increase of calcination temperature, the grain growth and crystallinity increase [44]. When the calcination temperature was further increased to 650 °C, a small portion of anatase in Fe/N/Co-TiO₂ began to be converted into a more stable rutile, which implied that the rutile transition temperature of Fe/N/Co-TiO₂ is between 600 and 650 °C.

3.1.4. The Effect of Calcination Temperature on the UV-Vis of Fe/N/Co-TiO₂

Figure 5 shows the UV-Vis of Fe/N/Co-TiO₂ prepared at different calcination temperatures. It was found that the UV-Vis spectra of Fe/N/Co-TiO₂ prepared at 550 and 600 °C were almost the same. This is because the crystal morphology of Fe/N/Co-TiO₂ anatase was improved, and the grain size increased with the increase of calcination temperature from 550 to 600 °C. Actually, perfect crystal form contributes to the increase of light absorption intensity, while coarse grain size inhibits the absorption and utilization of light by photocatalysts. Therefore, the absorbances of Fe/N/Co-TiO₂ calcined at 550 and 600 °C are basically the same under the above two effects.

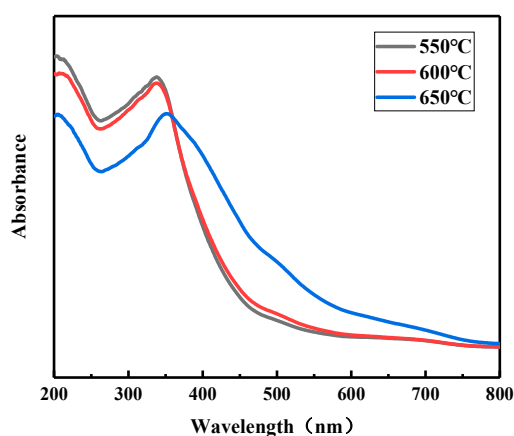


Figure 5. The UV-Vis spectra of Fe/N/Co-TiO₂ after calcination at different temperatures.

When the calcination temperature reaches 650 °C, the absorptive strength of Fe/N/Co-TiO₂ in the visible region is considerably improved, while the absorptive strength in the ultraviolet region is a fair amount lower than that after calcined at 550 and 600 °C. This phenomenon may be caused by a transformation between crystal forms. Some anatase is transformed into rutile, and rutile can be excited by light of a larger wavelength range than anatase to produce photoelectrons, but anatase has both higher light absorption and photocatalytic activity than rutile [45].

3.1.5. TEM of Fe/N/Co-TiO₂

Figure 6 shows the TEM images of the Fe/N/Co-TiO₂. It can be seen that the particle size of Fe/N/Co-TiO₂ ranges from 50 to 200 nm, and there is a certain degree of agglomeration (Figure 6a). According to the HR-TEM of Fe/N/Co-TiO₂ displayed in Figure 6a, the d-spacing was 0.351 nm, which corresponds to the (101) lattice planes of anatase TiO₂ [46]. Moreover, the SAED (inset) images in Figure 6b indicate the single-crystalline characteristics, which confirm that the results are consistent with XRD measurements.

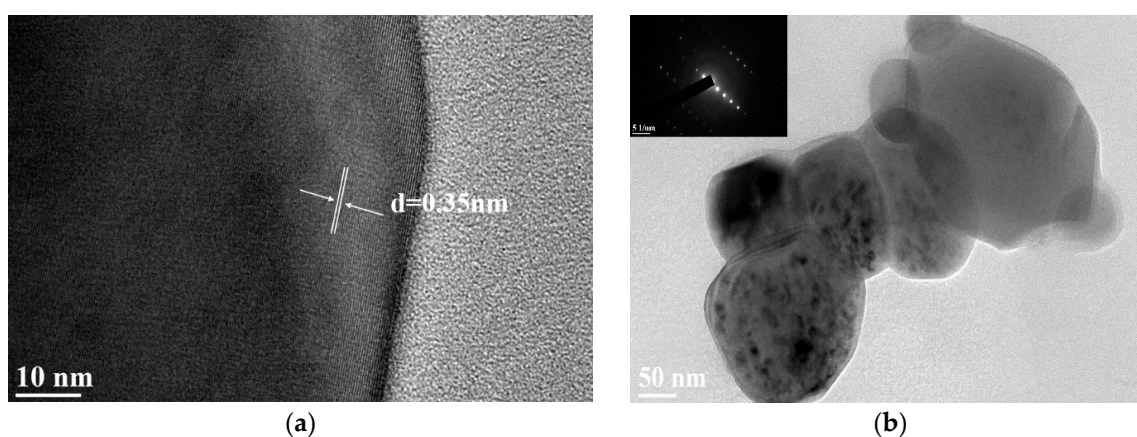


Figure 6. The HR-TEM (a) and TEM (b) images of Fe/N/Co-TiO₂ particles.

3.1.6. XPS Spectra of Fe/N/Co-TiO₂

The chemical compositions of Fe/N/Co-TiO₂ were further studied by XPS of Fe/N/Co-TiO₂ and TiO₂ NPs, as shown in Figure 7. The XPS of Fe/N/Co-TiO₂ mainly contained Ti, O, C, and other elements (Figure 7a). Among them, C 1s detected by 284.8 eV was caused by organic pollutants remaining during the preparation process [47]. Ti shows a strong peak position at 458.7 and 464.5 eV, as shown in Figure 7b. The two characteristic peaks correspond to Ti2p_{3/2} and Ti2p_{1/2}, respectively. The position where the peak of Ti in Fe/N/Co-TiO₂ appears with smaller shift and is deviated by 0.2 eV, showing higher photocatalytic activity, which is consistent with the results of UV test. The characteristic peaks of O 1s are asymmetrical according to Figure 7c. There are 530.0 and 532.2 eV peaks in Fe/N/Co-TiO₂, and 529.9 and 531.7 eV peaks in TiO₂. The peak of O 1s at 529.9 and 530.0 eV could be attributed to the O²⁻ anions of the TiO₂ crystalline lattice. 532.2 and 531.7 eV is the hydroxyl oxygen peak of -OH on the surface of Fe/N/Co-TiO₂ and TiO₂ [48]. The presence of surface -OH indicates that the Fe/N/Co-TiO₂ has catalytic degradation ability. This is because TiO₂ is an n-type semiconductor. When it is illuminated, the valence band electrons gain energy and jump to the conduction band to form photogenerated electrons; at the same time, holes are formed in the valence band. The -OH on the surface of TiO₂ are easily oxidized into -OH by holes, and the -OHs have extremely strong oxidation capacity, which can oxidize inorganic substances or most organic substances into inorganic small molecules, CO₂ and H₂O [48]. Compared with undoped TiO₂, the -OH peak of Fe/N/Co-TiO₂ was stronger, and it may be inferred that it has more excellent photocatalytic degradation.

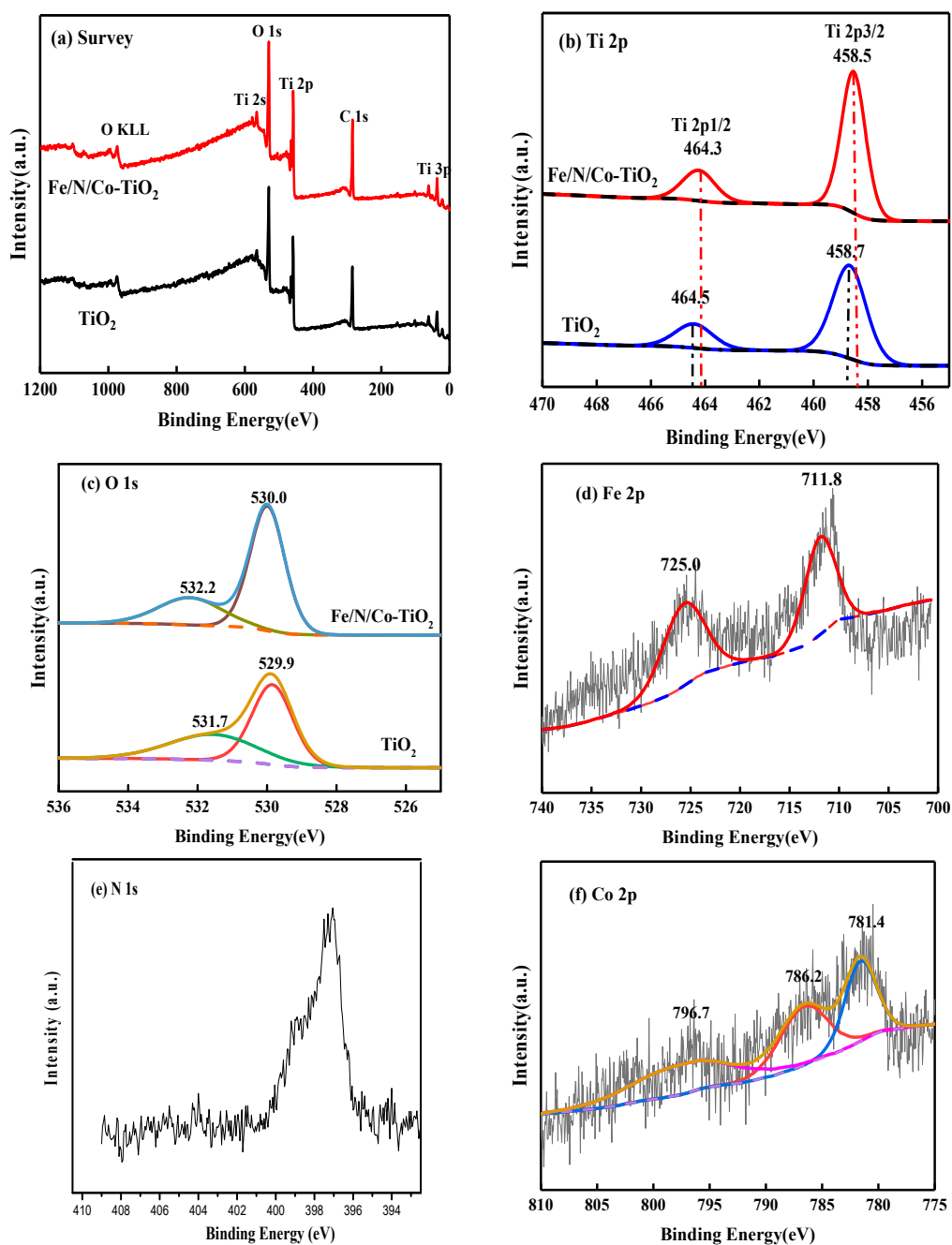


Figure 7. The XPS spectra: (a) survey, (b) Ti 2p, (c), O 1s, (d) Fe 2p, (e) N 1s, and (f) Co 2p of Fe/N/Co-TiO₂ and TiO₂ nanoparticles (NPs).

Figure 7d shows the Fe 2p spectra of Fe/N/Co-TiO₂. The two peaks of 711.8 and 725.0 eV appeared after the peak-fit processing of Fe 2p spectra, which correspond to Fe2p_{3/2} and Fe2p_{1/2}, indicating that Fe exists in the +3 valence state. In combination with the above XRD, there was no peak of Fe₂O₃, and the ionic radius (0.64 Å) of Fe³⁺ was similar to that of Ti⁴⁺ (0.68 Å) [49], so it was concluded that Fe³⁺ was successfully incorporated into the crystal lattice and formed Fe-O-Ti bonds. The XPS pattern fitting of N 1s found that only one characteristic peak appeared 397.0 eV (Figure 7e), indicating that O in a large number of N substituted TiO₂ lattices forms Ti-N bonds [50]. There are 781.4, 786.2, and 796.7 eV peak positions after the peak-fit processing of Co 2p spectra as can be seen in Figure 7f. Among them, the peak at 781.4 and 796.7 eV correspond to Co2p_{3/2} and Co2p_{1/2} of Co³⁺ respectively. The peak

at 786.2 eV corresponds to Co^{2+} , and the peak of CoO at 780.0 eV did not appear [51,52], indicating that Co^{3+} and Co^{2+} coexist in Fe/N/Co-TiO_2 and parts of Co replace Ti in the doped TiO_2 lattice.

3.2. The Photocatalytic Degradation Ability of the Photocatalyst

3.2.1. The Photocatalytic Degradation Performance of Fe/N/Co-TiO_2 on MB

In order to determine the photocatalytic activity of doped- TiO_2 prepared above, the MB solution was adopted and the results are shown in Figure 8. After 120 min of irradiation, Fe/N/Co-TiO_2 exhibited the highest catalytic degradation rate, which was 85%, followed by Fe/N-TiO_2 and Fe-TiO_2 , and finally, TiO_2 . The main reasons for the improvement of photocatalytic performance may be as follows: (i) Metal/nonmetal doping improves the visible light absorption intensity of TiO_2 [42]. (ii) The specific surface area of TiO_2 grain may increase, the MB molecules are more easily adsorbed on the surface, and the contact area is increased, thereby the degradation rate increases [43,53].

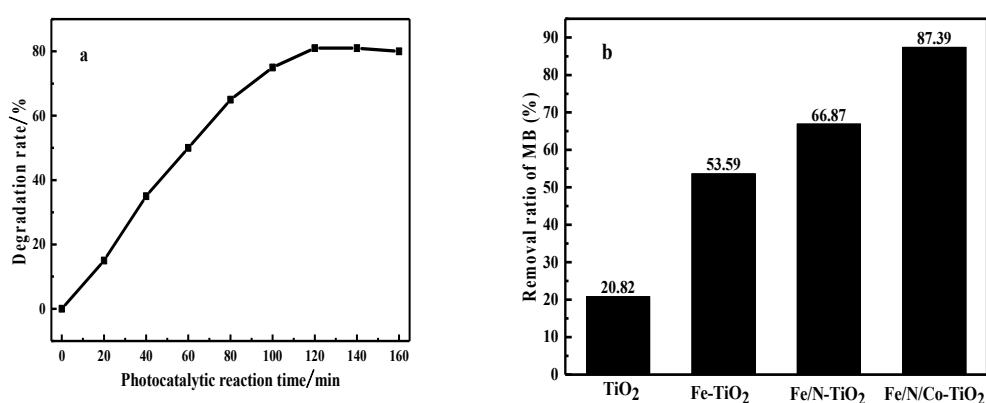


Figure 8. Methylene blue (MB) degradation experiment. (a) The variation of MB degradation efficiency with reaction time; (b) degradation rates for MB after 120 min under visible light irradiation.

3.2.2. The Photocatalytic Degradation Performance of Fe/N/Co-TiO_2 on VE

Figure 9 shows the photocatalytic degradation of three components in VE by Fe/N/Co-TiO_2 under visible light. As can be seen from Figure 9a, the concentration of NO_x decreased rapidly in the first half hour. After that, the concentration decline slowed down gradually. After 2 h, the concentration of NO_x was about 4 ppm, and the degradation efficiency was 71.04%. NO_x concentration decreased very slowly in the last 1 h. At the same time, the degradation efficiencies of CO and CO_2 remained almost unchanged, as depicted in the Figure 9b. Therefore, the late degradation of VE was carried out according to the irradiation time of 2 h. The decline of degradation performance may be due to the nitric acid and nitrates produced by oxidation of NO_x covered with a doped- TiO_2 surface [54]. The effective contact area between the exhaust gas and the photocatalyst was reduced. The increase in the CO_2 concentration of the inflection point in Figure 9b may be caused by the oxidation of part of CO to CO_2 [55].

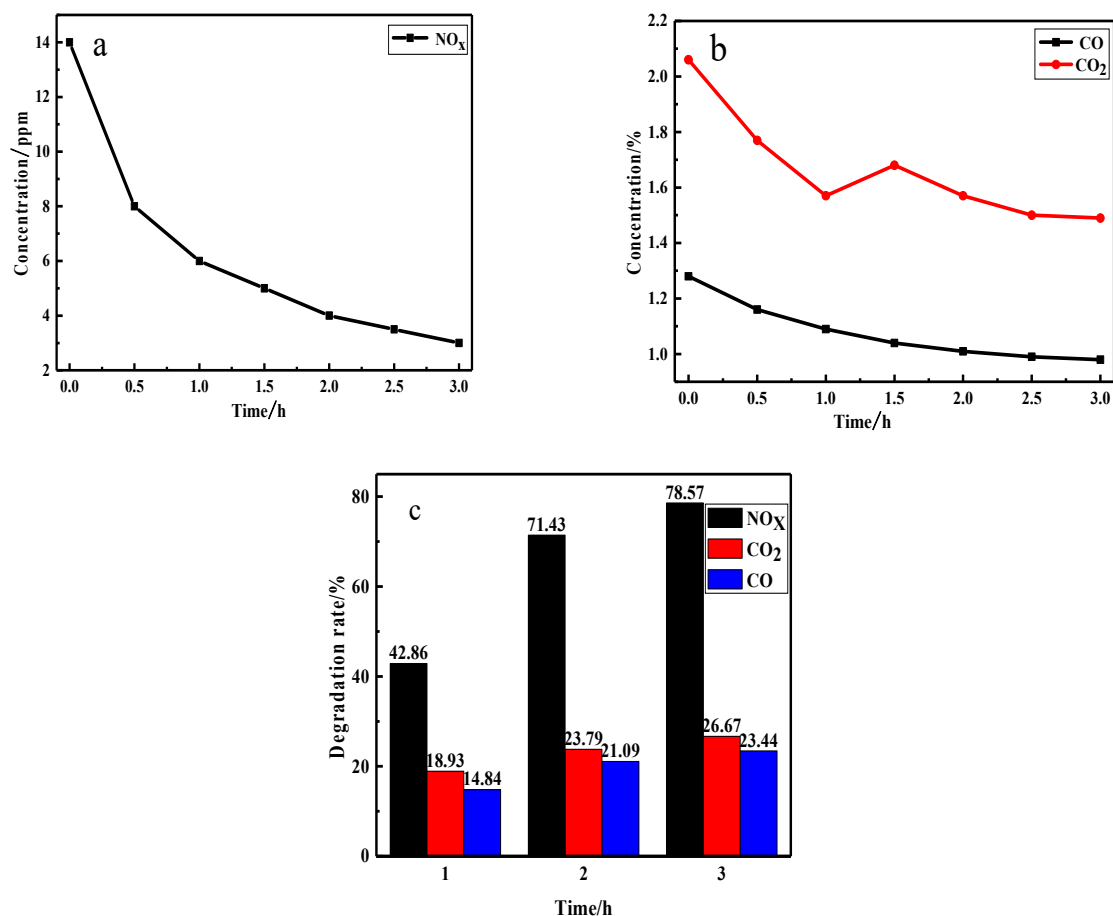


Figure 9. The concentrations of NO_x, (a) and CO and CO₂ (b) during the photocatalytic reaction process, and the photocatalytic degradation rate of VE (c) by doped TiO₂ under visible light.

3.3. The Elementary and Photocatalytic Performance of Photocatalytic Coating

3.3.1. The Elementary Performance of Photocatalytic Coating

In order to ensure the effective use of photocatalytic coatings, the elementary properties of the coatings were determined according to JG/T 512-2017 (General Technical Requirements for Building Exterior Wall Coatings) first. Test results are shown in the Table 2. It was found that the elementary properties of the coating met the code requirement (JG/T 512-2017), and the resistances to water, salt, and alkali were good.

Table 2. Elementary properties and corrosion resistance of photocatalytic coating.

Project	Pencil Hardness	Adhesive Strength	Water Resistance (168 h)	Salt and Alkali Resistance (168 h)
Coating	4H	1.15 Gpa (IV)	No abnormality (II)	No abnormality(III)

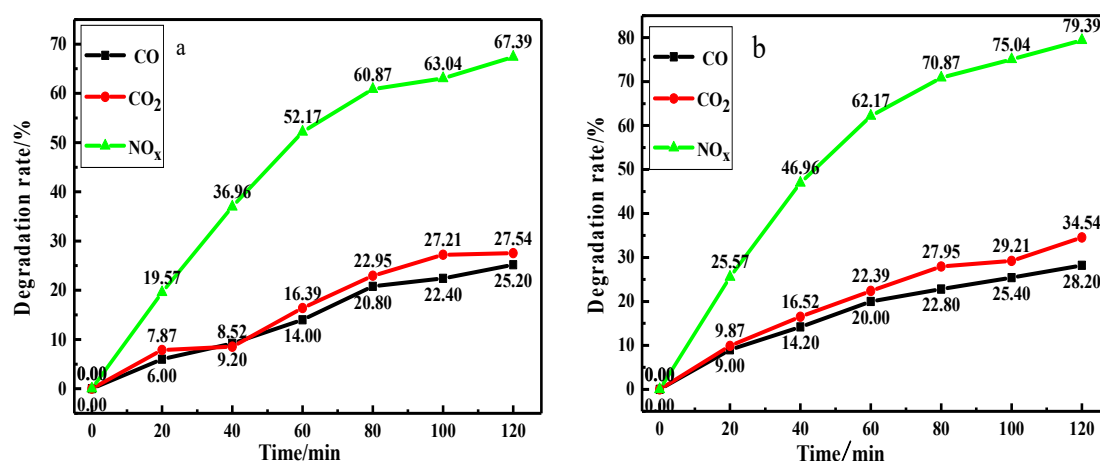
The durability of the coating can be evaluated by accelerated weather aging test (1000 h). To ensure test accuracy, three coated cotton-free fiber cement boards (labeled A, B, and C) were tested simultaneously; the results are shown in Table 3. After 6 weeks of exposure, the aging degree of the three samples can be neglected. The evaluation grade was Level 1, indicating that the photocatalytic coating meets code and construction requirements. The slight pulverization of the surface is mainly due to the photocatalytic degradation effect of the photocatalyst, which degrades the organic matter of the coating.

Table 3. The results of accelerated weather aging test (1000 h) for photocatalytic coating.

Sample	Discolouration	Pulverization	Cracking	Blistering	Damage	Evaluation Grade
A	1	1	0	0	1/S1	1
B	0	1	0	0	1/S1	1
C	1	1	0	0	1/S1	1

3.3.2. The Photocatalytic Degradation Performance of the Coating on VE

The photocatalytic degradation performance of the coating under different illumination conditions was studied, as shown in Figure 10. The degradation rates of NO_x , CO, and CO_2 under visible light were 67.39%, 25.20%, and 27.54%, respectively. In contrast, under ultraviolet irradiation, the degradation efficiencies were higher, 79.39%, 28.20%, and 34.54%, respectively. This phenomenon may be due to that the absorption intensity exhibited Fe/N/Co–TiO₂ in the ultraviolet region was higher than that of visible light (according to the UV-Vis results above). Furthermore, the energy of ultraviolet light is higher than that of visible light, and it is easier to generate more photoelectrons for photocatalytic reaction when Fe/N/Co–TiO₂ is irradiated [56]. It is obvious that photocatalytic coating is effective at degrading the main harmful gas in VE under visible light irradiation. At the same time, the higher degradation efficiency of the photocatalytic coating is related to the network structure of the acrylic substrate, which can effectively avoid the agglomeration of doped TiO₂ NPs [57,58].

**Figure 10.** The degradation rate of VE under (a) visible light and (b) ultraviolet light.

3.3.3. Reusability of the Photocatalytic Degradation

Reusability is an important indicator to evaluate the performance of photocatalytic coatings. Considering that photocatalytic coatings need to be cleaned frequently in practical use, some photocatalysts may lose their activity after repeated cleaning, resulting in the reduction of photocatalytic efficiency, so the influence of rinsing times on photocatalytic properties of coatings was investigated. The specific experimental process was as follows: firstly, a VE degradation test was carried out; after that, the coating was rinsed with tap water for 1 min to ensure that the surface of the coating was clean, then dry, at room temperature. The experiments were repeated ten times and the VE degradation test results were recorded (Figure 11).

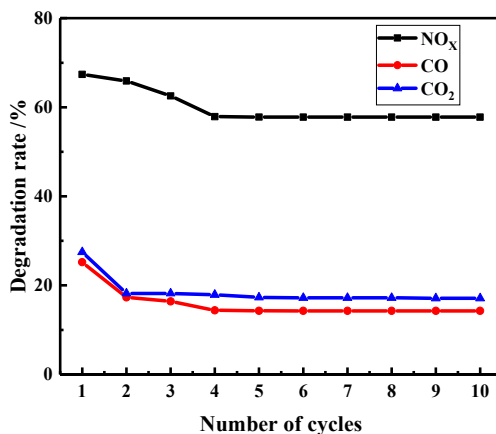


Figure 11. The reusability for VE degradation performance of photocatalytic coating.

It was found that with an increase in washing times, the degradation efficiency decreased first and then tended to be stable after four cycles. The degradation efficiencies of NO_x, CO, and CO₂ were slightly reduced between the first and fourth cycles. The decrease of degradation efficiency may be mainly attributed to two aspects. Firstly, with the prolongation of exposure time, as a small part of the effective photocatalytic material on the surface falls off. Secondly, during the rinsing process, a small amount of hydrophilic or water-soluble substances are not completely washed out, and remain in the pits and channels on the surface of the coating, which affects the adsorption of the coating to VE. However, after four cycles, the degradation rates of NO_x, CO, and CO₂ remained stable, demonstrating good reusability of the coating. This may be due to the confinement effect of the acrylic emulsion on doped TiO₂, which does not change the dispersion state of the doped TiO₂ on the surface of the coating during the scouring process [59].

3.3.4. Durability of the Photocatalytic Coating

Durability is an important index for long-term use of coatings. It can be evaluated by the exposure test. Firstly, the photocatalytic coating was coated on the surface of the cement boards, and then the cement boards were exposed to sunlight. It was stipulated that the test site is roof, and the test day had to be sunny. Finally, VE degradation performance was measured every two weeks; test results are shown in Figure 12.

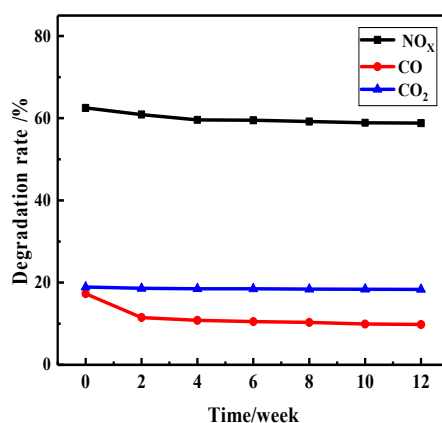


Figure 12. The durability for VE degradation performance of photocatalytic coating.

As shown in Figure 12, it can be seen that the photocatalytic coating showed a slight decrease in photocatalytic activity after natural exposure. The degradation rates of the coating on NO_x, CO and, CO₂ decreased by 3.7%, 7.5%, and 0.55% respectively, after 12 weeks. The main reason for this phenomenon may be that during the exposure test, the Fe/N/Co–TiO₂ has a slight degradation effect

on waterborne, acrylic substrate, resulting in a slight smashing of the surface of the coating and a small amount of photocatalyst falling off. In addition, the adsorbate on the surface of the coating may also cover the surface of the photocatalyst to affect its contact with VE [60]. However, due to the crosslinked structure of the coating and confinement effect on doped TiO₂, most photocatalysts still adhere to the surface/interior of the coating, showing excellent durability and can meet the requirements of normal use.

4. Conclusions

In this study, visible light responsive Fe/N/Co–TiO₂ nanoparticles with good photocatalytic activity were prepared. The effects of Fe, N, and Co doping on the crystal size, micro-structure, and photocatalytic performance of Fe/N/Co–TiO₂ were investigated. The degradation rates of NO_x, CO, and CO₂ in VE under visible light reached 71.43%, 23.79%, and 21.09%, respectively. Then, a visible-light-responsive and durable photocatalytic coating was constructed for degrading harmful gas in the VE by loading Fe/N/Co–TiO₂ particles into the waterborne acrylic coating. The coating exhibited efficient performance of visible light degradation for VE, and the degradation rates of NO_x, CO, and CO₂ reached 67.39%, 25.20%, and 27.54%. Furthermore, the photocatalytic coating exhibited favorable reusability and durability, due to the crosslinked structure in the coating and the confinement effect on doped TiO₂. It is believed that this study provides an efficient and simple method for the purification of VE in some special environments (such as tunnels) that only have visible light.

Author Contributions: H.X. and L.S. conceived and designed the experiments; G.L. and R.Z. participated in the experiments and measurements; L.S. and H.C. participated in the discussion of the results; H.X. and G.L. drafted the manuscript.

Funding: This work was supported by the Natural Science Foundation of China (grant number 51202016), the Special Fund for Basic Scientific Research of Central Colleges, Chang'an University (grant number 3001102319501), the Natural Science Basic Research Plan in Shaanxi Province of China (grant number 2017JQ2025), and the Xi'an Science and Technology Planning Project (grant number 2017137SF/WM031).

Conflicts of Interest: The authors declare no conflict of interest.

References

1. Zheng, Z.; Du, Z.; Yan, Q.; Xiang, Q. The impact of Rhythm-Based visual reference system in long highway tunnels. *Saf. Sci.* **2016**, *95*, 75–82. [[CrossRef](#)]
2. Keyte, I.; Albinet, A.; Harrison, R. On-Road traffic emissions of polycyclic aromatic hydrocarbons and their Oxy- and Nitro-Derivative compounds measured in road tunnel environments. *Sci. Total Environ.* **2016**, *566*, 1131–1142. [[CrossRef](#)] [[PubMed](#)]
3. Yang, F.; Gao, Y.; Zhong, K.; Kang, Y. Impacts of Cross-Ventilation on the air quality in street canyons with different building arrangements. *Build. Environ.* **2016**, *104*, 1–12. [[CrossRef](#)]
4. Lackovičová, A.; Guttová, A.; Bačkor, M.; Pišút, P.; Pišút, I. Response of Evernia prunastri to urban environmental conditions in Central Europe after the decrease of air pollution. *Lichenologist* **2013**, *45*, 89–100. [[CrossRef](#)]
5. Lacressonnière, G.; Watson, L.; Gauss, M.; Engardt, M.; Andersson, C.; Beekmann, M.; Colette, A.; Foret, G.; Josse, B.; Marecal, V.; et al. Particulate matter air pollution in Europe in a +2 °C warming world. *Atmos. Environ.* **2017**, *154*, 129–140. [[CrossRef](#)]
6. Guerreiro, C.; Foltescu, V.; De, L. Air quality status and trends in Europe. *Atmos. Environ.* **2014**, *98*, 376–384. [[CrossRef](#)]
7. Nieuwenhuijsen, M. Urban and transport planning, environmental exposures and Health-New concepts, methods and tools to improve health in cities. *Environ. Health* **2016**, *15*, 38. [[CrossRef](#)]
8. Stefania, S.; Marta, C.; Elena, I.; Flavia, V.; Hopke, P.; Rammazzo, G. Urban air quality in a Mid-Size City-PM_{2.5} composition, sources and identification of impact areas: From local to long range contributions. *Atmos. Res.* **2017**, *186*, 51–62. [[CrossRef](#)]
9. Leng, Z.; Yu, H. Novel method of coating titanium dioxide on to asphalt mixture based on the breath figure process for air-purifying purpose. *J. Mater. Civ. Eng.* **2015**, *28*, 52–59. [[CrossRef](#)]

10. Franklin, M.; Vora, H.; Avol, E.; McConnell, R.; Lurmann, F.; Liu, F.; Penfold, B.; Berhane, K.; Gilliland, F.; Gauderman, W. Predictors of intra-community variation in air quality. *J. Expo. Sci. Environ. Epidemiol.* **2012**, *22*, 135–147. [[CrossRef](#)]
11. Gao, X.; Hu, T.; Wang, K. Research on motor vehicle exhaust pollution monitoring technology. *Appl. Mech. Mater.* **2014**, *620*, 244–247. [[CrossRef](#)]
12. Zhao, Y.; Gao, P.; Yang, W.; Ni, H. Vehicle exhaust: An overstated cause of haze in China. *Sci. Total Environ.* **2018**, *612*, 490–491. [[CrossRef](#)] [[PubMed](#)]
13. Carneiro, J.; Teixeira, V.; Azevedo, S.; Neves, J. Development of photocatalytic ceramic materials through the deposition of TiO₂ nanoparticles layers. *J. Nano Res.* **2012**, *18*, 165–176. [[CrossRef](#)]
14. Gauderman, W.; McConnell, R.; Gilliland, F.; London, S.; Thomas, D.; Avol, R.; Vora, H.; Berhane, K.; Rappaport, T.; Lurmann, F.; et al. Association between air pollution and lung function growth in southern California children. *Am. J. Respir. Crit. Care Med.* **2000**, *166*, 76–84. [[CrossRef](#)] [[PubMed](#)]
15. Tang, Y.; John, C.; Eric, G. Agglomerated Activated Carbon Air Filter. U.S. Patent 5332426, 26 July 1994.
16. Laura, B.; Ilaria, A.; Andrea, L.; Giovanni, P.; Germana, B.; Giadad, G.; Paolo, M.; Simona, R.; Danilo, B.; Pier, P. Nanocrystalline TiO₂ coatings by Sol-Gel: Photocatalytic activity on Pietra di Noto biocalcarenite. *J. Sol-Gel Sci. Technol.* **2015**, *75*, 141–151. [[CrossRef](#)]
17. Liu, W.; Wang, S.; Zhang, J.; Fan, J. Photocatalytic degradation of vehicle exhausts on asphalt pavement by TiO₂/rubber composite structure. *Constr. Build. Mater.* **2015**, *81*, 224–232. [[CrossRef](#)]
18. Snapkauskienė, V.; Valinčius, V.; Grigaitienė, V. Preparation and characterization of TiO₂-Based Plasma-Sprayed coatings for NO_x abatement. *Catal. Today* **2012**, *191*, 154–158. [[CrossRef](#)]
19. Fujishima, A.; Hashimoto, K.; Watanabe, T. *TiO₂ Photocatalysis: Fundamentals and Applications*; BKC: Bombay, India, 1999; Volume 35, pp. 1137–1138. ISBN 4-939051-03-X.
20. Nelson, M.; Bohn, H. Soil-Based biofiltration for air purification: Potentials for environmental and space lifesupport application. *J. Environ. Prot. Ecol.* **2011**, *2*, 1084–1094. [[CrossRef](#)]
21. Wang, W.; Weng, X.; Wu, K.; Chen, G.; Zheng, G.; Wu, Z. Exploration of air pollutant purification technology for urban road tunnels. *Mod. Tunn. Tec.* **2014**, *51*, 41–48. (In Chinese) [[CrossRef](#)]
22. Vinodkumar, E.; Cristiana, D.; Jenny, S.; Detlef, B.; Suresh, C. Visible-Light activation of TiO₂ photocatalysts: Advances in theory and experiments. *J. Photochem. Photobiol. C-Photochem. Rev.* **2015**, *25*, 1–29. [[CrossRef](#)]
23. Scanlon, D.; Dunnill, C.; Buckeridge, J.; Shevlin, S.; Logsdail, S.; Woodley, S.; Catlow, C.; Powell, M.; Palgrave, R.; Parkin, I.; et al. Band alignment of rutile and anatase TiO₂. *Nat. Mater.* **2013**, *12*, 798–801. [[CrossRef](#)] [[PubMed](#)]
24. Shi, H.; Magaye, R.; Castranova, V.; Zhao, J. Titanium dioxide nanoparticles: A review of current toxicological data. *Part. Fibre Toxicol.* **2013**, *10*, 15. [[CrossRef](#)] [[PubMed](#)]
25. Xu, H.; Liu, L.; Sun, L. Research on the application of photocatalytic coating material with function of decomposing vehicle exhaust on road collision wall. *Adv. Mater. Res.* **2011**, *356–360*, 415–422. [[CrossRef](#)]
26. Pirola, C.; Boffito, D.; Vitali, S. Photocatalytic coatings for building industry: Study of 1 year of activity in the NO_x degradation. *J. Coat. Technol. Res.* **2012**, *9*, 453–458. [[CrossRef](#)]
27. Martinez, T.; Bertron, A.; Escadeillas, G.; Ringot, E.; Simon, V. BTEX abatement by photocatalytic TiO₂-bearing coatings applied to cement mortars. *Build. Environ.* **2014**, *71*, 186–192. [[CrossRef](#)]
28. Kanda, I.; Uehara, K.; Yamao, Y.; Yoshikawa, Y.; Morikawa, T. A Wind-Tunnel study on Exhaust-Gas dispersion from road Vehicles-Part II: Effect of vehicle queues. *J. Wind Eng. Ind. Aerodyn.* **2006**, *94*, 659–673. [[CrossRef](#)]
29. Gallusa, M.; Akylas, V.; Barmpas, F.; Beeldens, A.; Boonen, E.; Boreave, A.; Cazaunau, M.; Chen, H.; Daele, V.; Doussin, J.; et al. Photocatalytic De-Pollution in the Leopold II tunnel in Brussels: NO_x abatement results. *Build. Environ.* **2015**, *84*, 125–133. [[CrossRef](#)]
30. Guerrini, G. Photocatalytic performances in a city tunnel in Rome: NO_x monitoring results. *Constr. Build. Mater.* **2012**, *27*, 165–175. [[CrossRef](#)]
31. Torres-Carbajal, A.; Herrera-Velarde, S.; Castañeda-Priego, R. Brownian motion of a Nano-Colloidal particle: The role of the solvent. *Phys. Chem. Chem. Phys.* **2015**, *17*, 19557–19568. [[CrossRef](#)]
32. Dai, W.; Chen, X.; Li, E.; Li, E.; Wang, X.; Liu, P.; Fu, X. Influence of pH value of TiO₂ sol on surface gloss of corresponding TiO₂ film coated on ceramic tiles. *Surf. Eng.* **2009**, *25*, 106–110. [[CrossRef](#)]
33. Lai, L.; Wu, J. A facile solution approach to W, N Co-Doped TiO₂ nanobelt thin films with high photocatalytic activity. *J. Mater. Chem. A.* **2015**, *3*, 15863–15868. [[CrossRef](#)]

34. Phung, H.; Van, N.; Phuong, A.; Hung, V.; Nguyen, D. Effect of Co-Doping and Tri-Doping with transition metals and a nonmetal on photocatalytic activity in visible light of TiO₂ thin film. *J. Korean Phys. Soc.* **2017**, *70*, 995–1000. [[CrossRef](#)]
35. Fàbrega, C.; Andreu, T.; Cabot, A.; Morante, J. Location and catalytic role of iron species in TiO₂: Fe photocatalysts: An EPR study. *J. Photochem. Photobiol. A Chem.* **2010**, *211*, 170–175. [[CrossRef](#)]
36. Foura, G.; Chouchou, N.; Soualah, A.; Kouachi, K.; Guidotti, M.; Robert, D. Fe-doped TiO₂ supported on HY zeolite for solar photocatalytic treatment of dye pollutants. *Catalysts* **2017**, *7*, 344. [[CrossRef](#)]
37. Tong, T.; Zhang, J.; Tian, B.; Chen, F.; He, D. Preparation of Fe³⁺-doped TiO₂ catalysts by controlled hydrolysis of titanium alkoxide and study on their photocatalytic activity for methyl orange degradation. *J. Hazard. Mater.* **2008**, *155*, 572–579. [[CrossRef](#)] [[PubMed](#)]
38. Yang, K.; Ying, D.; Huang, B. Study of the nitrogen concentration influence on N-Doped TiO₂ anatase from First-Principles calculations. *J. Phys. Chem. C* **2007**, *111*, 12086–12090. [[CrossRef](#)]
39. Dolat, D.; Mozia, S.; Ohtani, B.; Morawski, A. Nitrogen, Iron-Single modified (N-TiO₂, Fe-TiO₂) and Co-Modified (Fe,N-TiO₂) rutile titanium dioxide as Visible-Light active photocatalysts. *Chem. Eng. J.* **2013**, *225*, 358–364. [[CrossRef](#)]
40. Altın, İ.; Sökmen, M.; Biyikloğlu, Z. Sol gel synthesis of cobalt doped TiO₂ and its dye sensitization for efficient pollutant removal. *Mater. Sci. Semicond. Process.* **2016**, *45*, 36–44. [[CrossRef](#)]
41. Dvoranová, D.; Brezová, V.; Mazúr, M.; Malati, M. Investigations of metal-doped titanium dioxide photocatalysts. *Appl. Catal. B Environ.* **2002**, *37*, 91–105. [[CrossRef](#)]
42. Cheng, X.; Yu, X.; Xing, Z. One-Step synthesis of Fe-N-S-Tri-Doped TiO₂ catalyst and its enhanced visible light photocatalytic activity. *Mater. Res. Bull.* **2012**, *47*, 3804–3809. [[CrossRef](#)]
43. Kim, T.; Glez, V.; Gyawali, G.; Cho, S. Synthesis of solar light responsive Fe, N Co-Doped TiO₂ photocatalyst by sonochemical method. *Catal. Today* **2013**, *212*, 75–80. [[CrossRef](#)]
44. Cheng, Y.; Luo, F.; Jiang, Y.; Li, F.; Wei, C. The effect of calcination temperature on the structure and activity of TiO₂/SiO₂, composite catalysts derived from titanium sulfate and fly ash acid sludge. *Colloid Surf. A Physicochem. Eng. Asp.* **2018**, *554*, 81–85. [[CrossRef](#)]
45. Yang, H.; Sun, C.; Qiao, S.; Zou, J.; Liu, G.; Smith, S.; Cheng, H.; Lu, M. Anatase TiO₂ single crystals with a large percentage of reactive facets. *Nature* **2008**, *453*, 638–641. [[CrossRef](#)] [[PubMed](#)]
46. Chowdhury, I.; Ghosh, S.; Naskar, M. Aqueous-Based Synthesis of Mesoporous TiO₂ and Ag-TiO₂ Nanopowders for Efficient Photodegradation of Methylene Blue. *Ceram. Int.* **2015**, *42*, 2488–2496. [[CrossRef](#)]
47. Tian, B.; Li, C.; Zhang, J. One-Step preparation, characterization and Visible-Light photocatalytic activity of Cr-Doped TiO₂ with anatase and rutile bicrystalline phases. *Chem. Eng. J.* **2012**, *191*, 402–409. [[CrossRef](#)]
48. Park, J.; Kim, S.; Bard, A. Novel Carbon-Doped TiO₂ nanotube arrays with high aspect ratios for efficient solar water splitting. *Nano Lett.* **2006**, *6*, 24–28. [[CrossRef](#)]
49. Pei, F.; Liu, Y.; Xu, S.; Lu, J.; Wang, C.; Cao, S. Nanocomposite of graphene oxide with nitrogen-doped TiO₂ exhibiting enhanced photocatalytic efficiency for hydrogen evolution. *Int. J. Hydrog. Energy* **2013**, *38*, 2670–2677. [[CrossRef](#)]
50. Zhang, A.; Long, L.; Liu, C.; Li, W.; Yu, H. Chemical recycling of the waste anodic electrolyte from the TiO₂ nanotube preparation process to synthesize Facet-Controlled TiO₂ single crystals as an efficient photocatalyst. *Green Chem.* **2014**, *16*, 2745. [[CrossRef](#)]
51. Tursun, R.; Su, Y.; Yu, Q.; Tan, J.; Hu, T.; Luo, Z.; Zhang, J. Effect of doping on the structural, magnetic, and ferroelectric properties of Ni_{1-x}A_xTiO₃ (A = Mn, Fe, Co, Cu, Zn; x = 0, 0.05, and 0.1). *J. Alloy. Compd.* **2019**, *773*, 288–298. [[CrossRef](#)]
52. Liu, X.; He, B.; Fu, B. Effects of doping cobalt on the structures and performances of TiO₂ photocatalyst. *Acta Chim. Sin.* **2008**, *14*, 1725–1730. (In Chinese) [[CrossRef](#)]
53. Du, Y.; Zheng, P. Adsorption and photodegradation of methylene blue on TiO₂-Halloysite adsorbents. *Korean J. Chem. Eng.* **2014**, *31*, 2051–2056. [[CrossRef](#)]
54. Ma, J.; Wu, H.; Liu, Y.; He, H. Photocatalytic removal of NO_x over visible light responsive Oxygen-Deficient TiO₂. *J. Phys. Chem. C* **2014**, *118*, 7434–7441. [[CrossRef](#)]
55. Zhu, H.; Qin, Z.; Shan, W.; Shen, W.; Wang, J. Pd/CeO₂-TiO₂ catalyst for CO oxidation at low temperature: A TPR study with H₂ and CO as reducing agents. *J. Catal.* **2004**, *225*, 267–277. [[CrossRef](#)]
56. Li, H.; Liu, J.; Qian, J.; Li, Q.; Yang, J. Preparation of Bi-Doped TiO₂ nanoparticles and their visible light photocatalytic performance. *Chin. J. Catal.* **2014**, *35*, 1578–1589. [[CrossRef](#)]

57. Wan, T. *Study on Titanium Dioxide-Polyacrylate Organic-Inorganic Hybrid Materials*; Sichuan University of China: Chengdu, China, 2006. (In Chinese)
58. Li, J.; Hong, X. Structure and properties of Nano-SiO₂/acrylic composite emulsion with interpenetrating networks prepared via Soap-Free emulsion polymerization. *J. Dispers. Sci. Technol.* **2010**, *31*, 5. [[CrossRef](#)]
59. Clement, J.; Alexandra, L.; Lisa, E.; Neil, C.; Richard, L.; Maria, C. Effect of weathering and traffic exposure on removal of nitrogen oxides by photocatalytic coatings on roadside concrete structures. *Mater. Struct.* **2015**, *48*, 3159–3171. [[CrossRef](#)]
60. Du, H. *Preparation and Performance of New Materials for Automobile Exhaust Purification in Tunnels*; Chang'an University of China: Xi'an, China, 2012. (In Chinese)



© 2019 by the authors. Licensee MDPI, Basel, Switzerland. This article is an open access article distributed under the terms and conditions of the Creative Commons Attribution (CC BY) license (<http://creativecommons.org/licenses/by/4.0/>).